Biomedical Optics EXPRESS

Achromatic miniature lens system for coherent Raman scattering microscopy

Richa Mittal, Mihaela Balu, Petra Wilder-Smith, and Eric O. Potma*

Beckman Laser Institute, University of California, Irvine, CA 92697, USA

*epotma@uci.edu

Abstract: We discuss the design and performance of a miniature objective lens optimized for coherent Raman scattering microscopy. The packaged lens assembly has a numerical aperture of 0.51 in water and an outer diameter of 8 mm. The lens system exhibits minimum chromatic aberrations, and produces coherent Raman scattering images with sub-micrometer lateral resolution (0.648 μm) using near-infrared excitation pulses. We demonstrate that despite the small dimensions of the miniature objective, the performance of this lens system is comparable to standard microscope objective lenses, offering opportunities for miniaturizing coherent Raman scattering imaging probes without sacrificing the image quality.

OCIS codes: (180.4315) Nonlinear microscopy; (350.3950) Micro-optics; (220.3630) Lenses.

References and links

1. J. X. Cheng and X. S. Xie, Eds., *Coherent Raman Scattering Microscopy* (CRC Press, 2013).
2. T. B. Huff and J. X. Cheng, "In vivo coherent anti-Stokes Raman scattering imaging of sciatic nerve tissue," J. Microsc. **225** 175–182 (2007).
3. F. P. Henry, D. Côté, M. A. Randolph, E. A. Z. Rust, R. W. Redmond, I. E. Kochevar, C. P. Lin, and J. M. Winograd, "Real-time in vivo assessment of the nerve microenvironment with coherent antiStokes Raman scattering microscopy," Plastic and reconstructive surgery **123**, 123S–130S (2009).
4. J. Zhu, B. Lee, K. K. Buhman, and J. X. Cheng, "A dynamic, cytoplasmic triacylglycerol pool in enterocytes revealed by ex vivo and in vivo coherent anti-Stokes Raman scattering imaging," J. Lipid Res. **50**, 1080–1089 (2009).
5. Y. Fu, W. Sun, Y. Shi, R. Shi, and J. X. Cheng, "Glutamate excitotoxicity inflicts paranodal myelin splitting and retraction," PLoS one **4**, e6705 (2009).
6. T. T. Le, H. M. Duren, M. N. Slipchenko, C. D. Hu, and J. X. Cheng, "Label-free quantitative analysis of lipid metabolism in living caenorhabditis elegans," J. Lipid Res. **51**, 672–677 (2010).
7. E. Bélanger, J. Crépeau, S. Laffray, R. Vallée, Y. De Koninck, and D. Côté, "Live animal myelin histomorphometry of the spinal cord with video-rate multimodal nonlinear microendoscopy," J. Biomed. Opt. **17**, 021107 (2012).
8. C. L. Evans, E. O. Potma, M. Puoris'haag, D. Côté, C. P. Lin, and X. S. Xie, "Chemical imaging of tissue in vivo with video-rate coherent anti-Stokes Raman scattering microscopy," Proc. Natl. Acad. Sci. USA **102**, 16807–16812 (2005).
9. B. G. Saar, C. W. Freudiger, J. Reichman,M. C. Stanley, G. Holtom, and X. S. Xie, "Video-rate molecular imaging in vivo with stimulated Raman scattering," Science **330** 1368–1370 (2010).
10. H. G. Breunig, R. Bückle, M. Kellner-Höfer, M. Weinigel, J. Lademann, W. Sterry, and K. König, "Combined in vivo multiphoton and CARS imaging of healthy and disease-affected human skin," Microsc. Res. Techn. **75**, 492–498 (2012).
11. C. Liang, K. B. Sung, R. R. Richards-Kortum, and M. R. Descour, "Design of a high-numerical-aperture miniature microscope objective for an endoscopic fiber confocal reflectance microscope," Appl. Opt. **41**, 4603–4610 (2002).
12. A. R. Rouse, A. Kano, J. A. Udovich, S. M. Kroto, and A. F. Gmitro, "Design and demonstration of a miniature catheter for a confocal microendoscope," Appl. Opt. **43**, 5763–5771 (2004).

#192404 - $15.00 USD Received 17 Jun 2013; revised 3 Aug 2013; accepted 23 Aug 2013; published 19 Sep 2013

13. M. D. Chidley, K. D. Carlson, R. R. Richards-Kortum, and M. R. Descour. "Design, assembly, and optical Bench testing of a high-numerical-aperture miniature injection-molded objective for fiber-optic confocal reflectance microscopy," Appl. Opt. **45**, 2545–2554 (2006).
14. H. J. Shin, M. C. Pierce, D. Lee, H. Ra, O. Solgaard, and R. Richards-Kortum, "Fiber-optic confocal microscope using a MEMS scanner and miniature objective lens," Opt. Express **15**, 9113–9122 (2007).
15. R. T. Kester, T. S. Tkaczyk, M. R. Descour, T. Christenson, and R. Richards-Kortum, "High numerical aperture microendoscope objective for a fiber confocal reflectance microscope," Opt. Express **15**, 2409–2420 (2007).
16. H. Bao, J. Allen, R. Pattie, R. Vance, and M. Gu, "Fast handheld two-photon fluorescence microendoscope with a 475 mm field of view for in vivo Imaging," Opt. Lett. **33**, 1333–1335 (2008).
17. R. P. J. Barretto, B. Messerschmidt, and M. J. Schnitzer, "In vivo fluorescence imaging with high-resolution microlenses," Nat. Meth. **6**, 511–512 (2009).
18. Y. Wu, J. Xi, M. J. Cobb, and X. Li, "Scanning fiber-optic nonlinear endomicroscopy with miniature aspherical compound lens and multimode fiber collector," Opt. Lett. **34**, 953–955 (2009).
19. M. Kyrish, U. Utzinger, M. R. Descour, B. K. Baggett, and T. S. Tkaczyk, "Ultra-slim plastic endomicroscope objective for non-linear microscopy," Opt. Express **19**, 7603–7615 (2011).
20. D. R. Rivera, C. M. Brown, D. G. Ouzounov, I. Pavlova, D. Kobat, W. W. Webb, and C. Xu, "Compact and flexible raster scanning multiphoton endoscope capable of imaging unstained tissue," Proc. Natl. Acad. Sci. USA **108**, 17598–17603 (2011).
21. H. Wang, T. B. Huff, Y. Fu, K. Y. Jia, and J. X. Cheng, "Increasing the imaging depth of coherent anti-Stokes Raman scattering microscopy with a miniature microscope objective," Opt. Lett. **32**, 2212–2214 (2007).
22. S. Murugkar, B. Smith, P. Srivastava, A. Moica, M. Naji, C. Brideau, P. K. Stys, and H. Anis, "Miniaturized multimodal CARS microscope based on MEMS scanning and a single laser source," Opt. Express **18** 23796–23804 (2010).
23. J. Knittel, L. Schnieder, G. Buess, B. Messerschmidt, and T. Possner, "Endoscope-compatible confocal microscope using a gradient index-lens system," Opt. Commun. **188**, 267–73 (2001).
24. C. J. Engelbrecht, R. S. Johnston, E. J. Seibel, and F. Helmchen, "Ultra-compact fiber-optic two-photon microscope for functional fluorescence imaging in vivo," Opt. Express **16**, 5556–5564 (2008).
25. J.C. Jung, A. D. Mehta, E. Aksay, R. Stepnoski, and M. J. Schnitzer, "In vivo mammalian brain imaging using one-and two-photon fluorescence microendoscopy," J. Neurophys. **92**, 3121–3133 (2004).
26. M. J. Levene, D. A. Dombeck, K. A. Kasischke, R. P. Molloy, and W. W. Webb, "In vivo multiphoton microscopy of deep brain tissue," J. Neurophys. **91**, 1908–1912 (2004).
27. L. Fu and M. Gu, "Double-clad photonic crystal fiber coupler for compact nonlinear optical microscopy imaging," Opt. Lett. **31**, 1471–1473 (2006).
28. B. A. Flusberg, A. Nimmerjahn, E. D. Cocker, E. A. Mukamel, R. P. J. Barretto, T. H. Ko, L. D. Burns, J. C. Jung, and M. J. Schnitzer, "High-speed, miniaturized fluorescence microscopy in freely moving mice," Nat. Meth. **5**, 935–938 (2008).
29. B. G. Saar, R. S. Johnston, C. W. Freudiger, X. S. Xie, and E. J. Seibel, "Coherent Raman scanning fiber endoscopy," Opt. Lett. **36**, 2396–2398 (2011).
30. C. S. Rim, "The optical design of miniaturized microscope objective for CARS imaging catheter with fiber bundle," J. Opt. Soc. Korea **14** 424–430 (2010).
31. Y. Jung, L. Tong, A. Tanaudommongkon, J. X. Cheng, and C. Yang, "In vitro and in vivo nonlinear optical imaging of silicon nanowires," Nano Lett. **9**, 2440-2444 (2009).

1. Introduction

Coherent Raman scattering (CRS) microscopy is a nonlinear optical imaging technique, including both coherent anti-Stokes Raman scattering (CARS) and stimulated Raman scattering (SRS), which provides label-free, molecular selective contrast at fast image acquisition rates. [1] A number of examples illustrate the potential of CRS for *in vivo* biomedical research. For instance, CRS has been used for studying lipid abnormalities in superficial tissues and in tissues accessible through minimally invasive surgery. [2–7] In addition, a potential to examine structures and topically applied drugs in skin *in vivo* has been shown. [8–10] Such studies underline the clinical potential of CRS microscopy. However, the practical translation of CRS techniques into a clinical setting is accompanied by several technological challenges. One of these challenges is the engineering of robust and small optical probes that can be directed to accessible parts of the body, including hollow tracts of the human body. Traditional microscope optical elements are not optimized for this purpose. In particular, the physical dimensions of the microscope objective lens, with diameters of typically 2 – 4 cm, are incompatible with the

#192404 - $15.00 USD Received 17 Jun 2013; revised 3 Aug 2013; accepted 23 Aug 2013; published 19 Sep 2013

design criteria of a lightweight and flexible probe.

In order to incorporate a focusing element with a high numerical aperture (NA) in small optical probes, miniaturization of optical components is required. Advances in this area can be divided into two categories: objective lens systems that use miniature multi-lens objectives and systems based on the use of gradient refractive index (GRIN) optics. Multi-lens miniature objectives have been used for linear and nonlinear imaging techniques such as confocal reflectance [11–15], two-photon excitation fluorescence (TPEF) [16–20] and CARS. [21, 22] Similarly, GRIN lenses have been utilized in confocal reflectance [23], TPEF [24–28] and CRS [29] imaging applications.

The design criteria for miniaturizing the focusing element in CRS microscopy are particularly challenging. CRS microscopy uses two excitation beams of different wavelength, which need to be focused to the same focal spot for optimum resolution and signal generation. This implies that, relative to other nonlinear optical imaging techniques such as TPEF, the suppression of chromatic aberrations is pertinent in CRS probe development. The necessity to minimize chromatic aberrations puts particular constrains on the lens design, requiring design parameters that are currently not trivially met in GRIN lens systems. [30] In terms of suppressing chromatic distortions in practice, multi-lens systems exhibit more flexibility as additional lenses can be incorporated to reach acceptable levels of achromaticity. [30]

Concurrently, the lens system needs to be designed for use in aqueous media, exhibit a high NA, feature an acceptable field of view and its physical dimensions should be compatible with the use of a small fiber-coupled probe. Despite significant advances made in this area, the performance of miniature lenses for CRS imaging has been inferior to the performance of commercially available, aberration-corrected microscope objectives. In this contribution, we discuss the design and imaging performance of a miniature multi-lens focusing system that meets the criteria mentioned above, and achromaticity in particular. By engineering the system specifically for minimum chromatic aberrations, excellent focusing parameters are obtained for both excitation beams, producing high-resolution CRS images with contrast comparable to conventional objective lenses.

2. Materials and methods

2.1. Miniature objective design

We used ZEMAX software for optical design of the lens system. The basic layout of the miniature objective design follows the design of standard microscope objectives, which consist of multiple lens components. Our design consists of 6 elements including a glass coverslip, forming a lens system that is optimized for water immersion and exhibits a NA of 0.51, see Fig. 1(a). The design makes use of achromatic and aspheric surface lens elements to compensate for various aberrations. The basic arrangement uses a thick meniscus negative component oriented convex towards the positive components. The first element (L1) is a 4.5 mm diameter lens (Cat# 67595, Edmund Optics) used to collimate the beam from a point source. This first element can be removed in case the objective is illuminated with collimated beams, in which case the lens system is compatible with an infinity corrected imaging system. The second lens (L2) is a custom-made negative achromatic lens. Its main purpose is to diverge the beam and improve the NA of the system. This lens element is fabricated by JenOptik according to our design specifications. The third and fourth lenses (L3, L4) are positive lenses consisting of two cemented achromatic doublets (Cat# 49923, Edmund Optics), followed by an aspheric singlet (L5, Cat# 355390, Lightpath technologies). The cemented achromatic doublets are made from two different glass materials to correct for chromatic aberrations of the pump and Stokes beams, while the aspheric lens located near the object mainly compensates monochromatic wavefront errors such as spherical aberrations and coma. Incorporation of a single aspheric lens replaced multi-

#192404 - $15.00 USD Received 17 Jun 2013; revised 3 Aug 2013; accepted 23 Aug 2013; published 19 Sep 2013

ple spherical optical lenses in the design, resulting in a more compact objective. The microscope objective is designed for use with a coverslip (L6), which protects the lens from moisture and external damage. The glass thickness of the coverslip contributes a significant amount of spherical aberrations and coma, which are compensated in the design calculations. The objective is corrected for chromatic aberrations over the spectral range from 810 nm to 1064 nm.

The objective design has a working distance of 0.872 mm. The maximum diameter of the lens system is 5.0 mm. To fix the lens positions, the elements are housed in a home-made brass sheath. Figure 1(b) shows a rendering of the components in the packaged objective. The physical length of the fully packaged objective is 19 mm and the outer diameter is 8.0 mm, see Fig. 1(c). To test the image quality of aberration corrected miniature objective, a comparison is made with an uncorrected aspheric singlet lens (Cat# 87165, Edmund Optics) and a commercial objective with a comparable NA (Plan-Neofluar 20X, 0.5 NA, Zeiss). The summary of the design specifications of the three lens systems is given in Table I.

Table 1. Specifications and experimental lateral resolution of the packaged miniature objective, the aspheric lens, and the commercial objective lens. Lateral resolution is given for the CARS imaging mode.

Specifications	**Miniature Objective**		**Aspheric**		**Zeiss Plan-Neofluar**		**Units**
NA	0.51		0.68		0.50		
Outer Diameter	8.0		6.33		24.0		mm
Working Distance	0.872		1.76		2.0		mm
Lateral Resolution	0.65 ± 0.07		1.00 ± 0.16		0.63 ± 0.06		μm
FOV	190×190		235×235		635×635		μm^2
Immersion	Water		Dry		Dry		
Coverslip	Yes (0.17)		No		Yes (0.17)		mm
Transmission	817 nm	1064 nm	817 nm	1064 nm	817 nm	1064 nm	
	55	23	72	47	62	43	%

2.2. Experimental layout

The experiments in this work were carried out with a pump wavelength of 817 nm and a Stokes wavelength of 1064 nm. The Stokes beam was derived from a Nd:vanadate laser (PicoTrain, HighQ Lasers), which produces ∼10 ps pulses at 76 MHz. We tested the performance of the lens with two different sources of the pump beam, producing either ps pulses or fs pulses. The ps pump pulses were derived from an optical parametric oscillator (Levante Emerald, APE), producing tunable 7 ps pulses in the 760–960 nm range. The fs pulses were generated by a Ti:sapphire laser (Mira-900, Coherent), which delivers 150 fs pulses tuned to 817 nm. The Nd:vanadate laser was electronically synchronized to the Ti:sapphire laser, yielding time-synchronized pump and Stokes pulses with a temporal jitter less than 0.500 ps.

Imaging studies were performed by integrating the lens in an imaging setup consisting of a laser scanning system and an optical detector. Briefly, the scanning system consisted of two computer controlled galvanometric mirrors (Fluoview 300, Olympus), a scan lens (f = 70) and a tube lens (f = 180mm). Because the imaging system was infinity corrected, L1 was removed to accommodate the collimated excitation beams at the back aperture of the miniature objective. The nonlinear signal was detected both in the forward and in the epi-direction. In the forward direction, the CARS signal was captured by a condenser, filtered by a bandpass filter (650 nm, Semrock), and detected by a photomultiplier tube (R3896, Hamamatsu). In the epi-direction, the signal was separated from the incident light with a dichroic mirror (760SWP, Chroma), filter by a bandpass filter and detected with an identical photomultiplier tube. The second harmonic

#192404 - $15.00 USD Received 17 Jun 2013; revised 3 Aug 2013; accepted 23 Aug 2013; published 19 Sep 2013

generation signal was detected by replacing the filter with a 400 nm bandpass filter (400 nm, Semrock). For the SRS experiments, the Stokes beam was amplitude modulated at 10 MHz with an acoustic optic modulator (Crystal Technologies). The stimulated Raman loss (SRL) signal was detected in the forward direction at the pump wavelength by a photodiode (FDS1010, Thorlabs), and the signal was demodulated with a home-built lock-in amplifier.

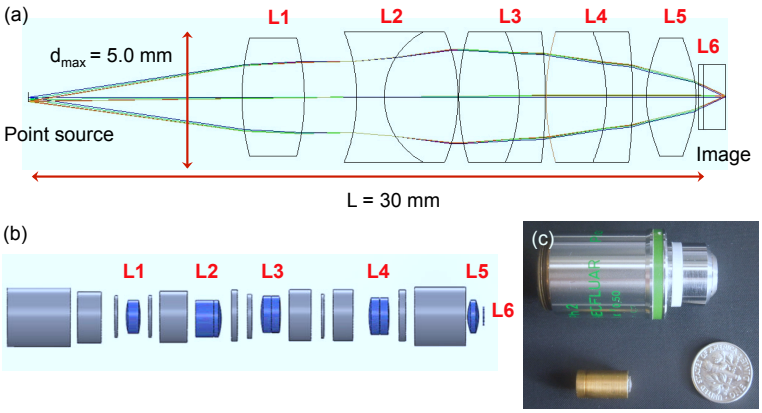

Fig. 1: Aberration corrected miniature objective. (a) Optical ray diagram of multiple lens elements combined to form a 5mm diameter, 0.51 NA miniature objective lens. (b) Rendering of the lenses and brass holder components (8 mm total outer diameter) with rings supporting lenses on both sides. (c) Photograph of the fabricated and assembled miniature objective next to a commercial objective.

2.3. Materials

30 nm diameter Si nanoparticles (Meliorum Technologies, Inc.) were used for lateral resolution measurement. The electronic four-wave mixing signal from the Si particles was used to visualize the focal width. [31] For axial resolution measurements, 1 μm diameter polystyrene beads (Polysciences, Inc.) were used. The samples were suspended in water, sonicated and embedded in an agraose gel. To test the capability of the miniature objective to image biological tissues, we imaged a freshly excised mouse ear (SAMP-8 mice) and rabbit skin (Pathogen-free New Zealand White rabbits Western Oregon Rabbit) tissue. In addition, to measure the imaging penetration depth of the microscope objectives we utilized turkey breast tissue. The samples were mounted directly on the coverslip for the imaging studies.

3. Results

The primary design criteria for the miniature CRS objective lens are minimum chromatic aberration and a high numerical aperture. These design criteria enable tight focusing of the pump and Stokes beams to a near diffraction-limited focal spot. Some common metrics of image quality are: the root-mean-square (r.m.s) radius of the spot size, the modulation transfer function (MTF), the Strehl ratio and the point spread function. Figure 2(a) shows the geometric spot diagram determined by optical ray tracing through the objective lens for different incident angles of the collimated beams. The Fig. illustrates the pattern of rays on the image plane at the optical axis (0 μm) and 50 μm off axis. The geometrically approximated Airy radius, determined at the midway wavelength of 950 nm, is indicated by the black circle in the image. The predicted root-mean square (r.m.s) radius value, on-axis is 0.421 μm and 50 μm off axis is 0.753 μm. The transverse chromatic error at 50 μm off axis is 0.235 μm (for 817 nm) and 0.146 μm (for

#192404 - $15.00 USD Received 17 Jun 2013; revised 3 Aug 2013; accepted 23 Aug 2013; published 19 Sep 2013

1064 nm). The lateral color error and the geometric spot size radius of the propagating rays remains within the estimated Airy disk, thus maintaining near diffraction-limited performance. The color-coded rays represent the different wavelengths (blue: 817 nm and red: 1064 nm). The axial chromatic error between the wavelengths is estimated as a maximum chromatic focal shift in the range of 1.29 μm, which is well below the diffraction-limited value of 3.22 μm. This microscope objective is well corrected for the on-axis aberrations, the dominating form of aberration is off-axis non-symmetric coma wavefront distortion, which increases with distance from the principal axis.

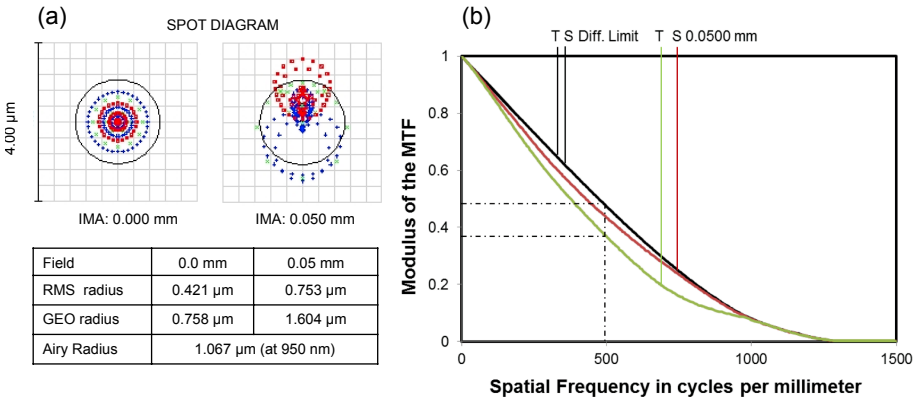

Field	0.0 mm	0.05 mm
RMS radius	0.421 µm	0.753 µm
GEO radius	0.758 µm	1.604 µm
Airy Radius	1.067 µm (at 950 nm)	

Fig. 2: ZEMAX predicted performance of the objective design. (a) Geometric spot size diagram for two radial distances from the optical axis (blue: 817 nm, red: 1064 nm wavelength). (b) Modulation transfer function (MTF) plot.

Figure 2(b) shows the modulation transfer function (MTF) plot, which represents the ability of the objective lens to transfer contrast of an ideal image to the actual image at a specific resolution. The graph depicts the image modulation as a function of line pairs per mm (lp/mm) for the image height of 50 μm from the principal axis. The solid black line shows the diffraction-limited performance for the miniature objective representing a contrast of 48% for 0.5 lp/μm. The objective performance is predicted close to the diffraction limit curve, with most deviation near the edge of the 100 μm field of view, with 38% contrast for 0.5 lp/μm. The Strehl ratio is another measurement of the objective lens performance and represents the illumination at the center of the diffraction pattern of an aberrated image, relative to that of an aberration-free image. The on axis and off axis (50 μm) Strehl ratio for the miniature objective are 0.968 and 0.86 respectively. The ratio indicates an acceptable level of wavefront aberration within the diffraction-limited image.

Figure 3 summarizes the imaging performance of the lens at the two fundamental excitation wavelengths. In Fig. 3(a), a transmission image of a high-resolution United States Air force (USAF) 1951 target is shown for the 817 nm excitation wavelength. Figure 3(b) shows the intensity profile of the cross section taken at group 9, element 1 as shown by the red line in (a). The width of each line is 0.98 μm, and the separation between lines is 0.98 μm. This image test shows that the objective is capable of resolving (sub-)micrometer structures in the one-photon imaging mode. Figures 3(c,d) show comparable results for the imaging performance at 1064 nm, albeit of slightly lower resolution because of the longer wavelength. An impression of the uniformity across the FOV is given in Fig. 3(e), where a Ronchi ruling is visualized with 817 nm in transmission mode. The straightness of the lines is an indication that field distortions are relatively minor. In Fig. 3(f) the lateral deviation is depicted, showing that distortion in the image is only a few μm across the entire FOV. Note that the field distortion is a combination of

#192404 - $15.00 USD Received 17 Jun 2013; revised 3 Aug 2013; accepted 23 Aug 2013; published 19 Sep 2013

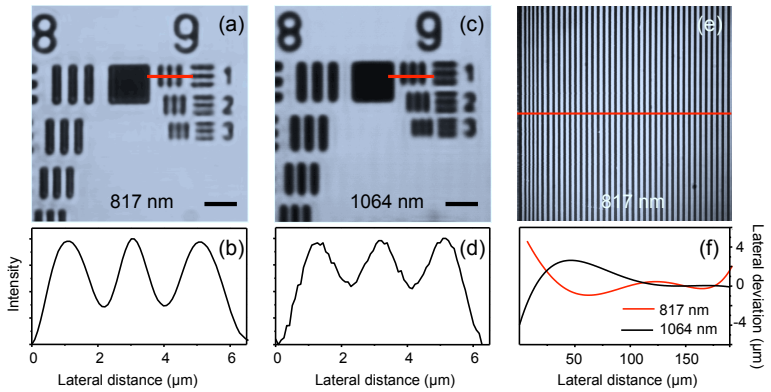

Fig. 3: Transmission images taken at the fundamental excitation wavelengths. (a) High-resolution USAF 1951 target visualized at 817 nm. (b) Cross section taken at the red line in (a). Scale bar is 5 μm. (c) USAF 1951 target visualized at 1064 nm. (d) Cross section taken at the red line in (c). Scale bar is 5 μm. (e) Ronchi ruling with 5 μm per line pair visualized at 817 nm. (e) Lateral deviation across the field of view for both excitation wavelengths.

the characteristics of both the objective lens as well as the extended scanning optics.

Table 2. Axial and lateral focal widths of the miniature objective in the CARS imaging mode.

Miniature Objective	**Lateral (FWHM)**	**Axial (FWHM)**	**Unit**
Theoretical	0.530	3.2	μm
Experimental	0.648	4.9	μm

While the one-photon imaging test provides useful information about the focusing quality of the objective, the actual CRS resolution depends on the focal volumes of both excitation beams. To determine the lateral resolution of the objective in the CARS modality, we imaged 30 nm diameter Si nanoparticles embedded in an agarose gel with both beams incident on the sample. The full-width-at-half-maximum (FWHM) of the CARS excitation volume was found at 0.648 $\pm$ 0.073 μm), see Fig. 4(a). The axial resolution was determined from a three-dimensional image of 1 μm diameter polystyrene beads, acquired with a 300 nm axial step size increment. Fitting the axial profiles of the beads to a Gaussian function, an axial FWHM of 4.9 $\pm$ 0.16 μm was obtained, see Fig. 4(b). A comparison with the theoretical values of the point spread function for aberration-free system is shown in Table II.

To test the image quality of the aberration corrected miniature objective, a comparison is made with an uncorrected miniature aspheric singlet lens and a commercial objective. The miniature aspheric lens was chosen to illustrate the performance of typical off-the-shelf miniature optics used for monochromatic optical probe designs. The commercial microscope objective is an achromatic lens system with a similar NA to our miniature objective. The performance of the commercial system serves as a direct comparison with the performance of the miniature CRS objective lens. The design specifications and the experimentally determined lateral resolution of each of the lens system are summarized in Table 1. It can be seen that the chromatically corrected miniature objective lens exhibits excellent confinement and overlap of the focused beams, producing a high spatial resolution.

For the comparison of the CARS image quality over the extended field of view for each of the lens systems we imaged the distribution of 16 μm polystyrene beads. The miniature

#192404 - $15.00 USD Received 17 Jun 2013; revised 3 Aug 2013; accepted 23 Aug 2013; published 19 Sep 2013

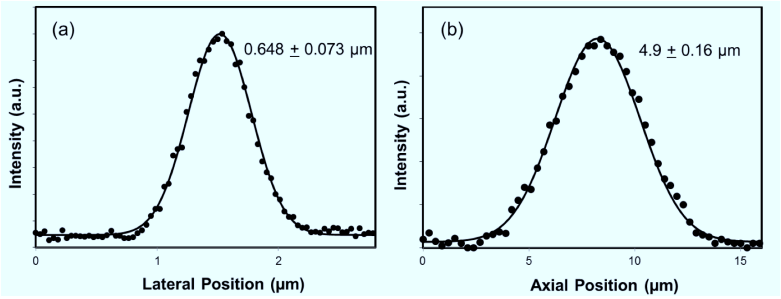

Fig. 4: Resolution measurement of the miniature objective lens. (a) Lateral and (b) axial CARS intensity profile measurement for a 0.51 NA miniature objective. FWHM values (0.648 ± 0.073 μm lateral; 4.9 ± 0.16 μm axial) were determined by averaging the results from n = 11 particles. The pump and stokes laser wavelength was 817 nm and 1064 nm, respectively, corresponding to a Raman shift of 2845 cm^{-1}. The pump and Stokes laser power at the sample are 10 mW and 20 mW respectively.

objective reveals a high quality image that appears undistorted within the field of view, as shown in Fig. 5(a). We attribute these favorable imaging properties to the reduced level of chromatic aberrations. In contrast, the conventional aspheric lens is uncorrected for aberrations and shows non-uniform image quality within the field of view, see Fig. 5(b). Such distortions can be attributed to variations in the overlap of the pump and Stokes beams in the focal plane as the beams are angularly adjusted at the back aperture of the focusing lens. We note that even at increased illumination powers the image quality of the aspheric lens remained poor. In addition, the images obtained with the miniature objective were compared with the commercial objective, shown in Fig. 5(c). The CRS image quality for the commercial lens and the miniature objective is comparable. However, as shown in Table I, the useable field of view of the commercial objective is significantly larger at 635 x 635 μm versus that of the miniature objective at 190 x 190 μm. Hence, the expansion of the FOV for the miniature objective is a future design challenge.

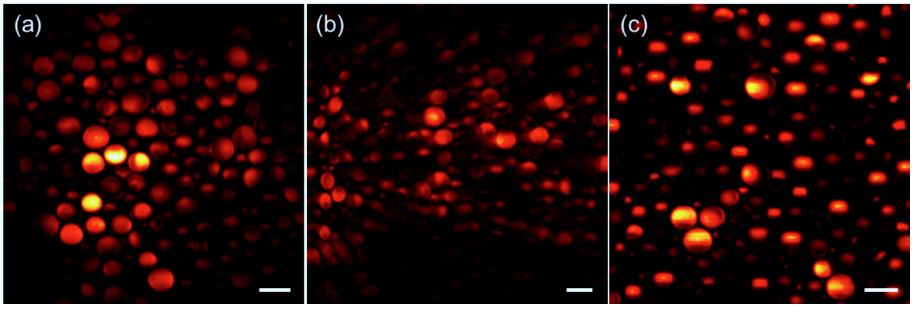

Fig. 5: CARS images of 16 μm polystyrene beads over an extended field of view. (a) Image of beads acquired with the 0.51 NA miniature objective. (b) Image obtained with the 0.6 NA aspheric lens. (c) Image acquired using the Zeiss, 20X, 0.5NA objective lens. A fs pump source was used. All images are 512 x 512 pixels. Scale bar is 20 μm

We have performed CARS imaging studies on mouse ear tissue to test the usefulness of the miniature objective for biomedical imaging. The lasers were tuned to the CH_2 vibrational stretch of lipids. Figure 6 shows representative images acquired with the custom-made objective

#192404 - $15.00 USD Received 17 Jun 2013; revised 3 Aug 2013; accepted 23 Aug 2013; published 19 Sep 2013

lens at various locations in the tissue. Several tissue components, including adipocytes in the subcutaneous layer (Fig. 6(a,b)), stratum corneum (Fig. 6(c)) and hair structures (Fig. 6(d)) are observed with excellent resolution and with high contrast.

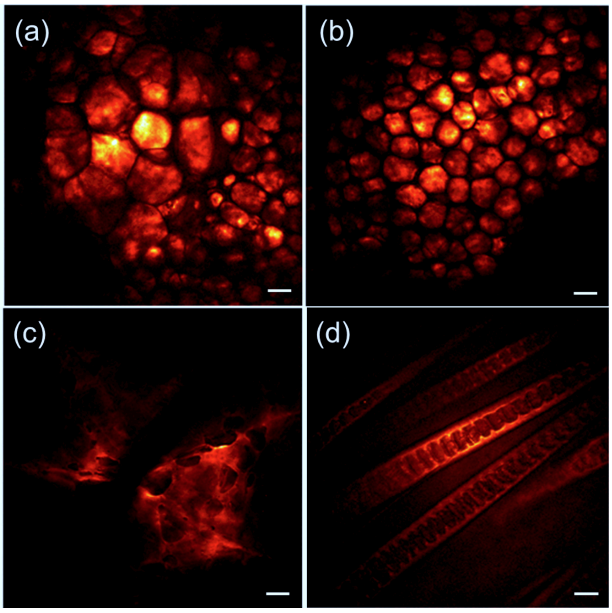

Fig. 6: CARS imaging of mouse ear tissue using the miniature objective lens at 2845 cm^{-1}. (a, b) Adipocytes of the subcutaneous layer at $\sim$80 μm from the skin surface. (c) Lipid contrast from the stratum corneum (d) Hair structures near the surface of the tissue. The pump and Stokes laser power at the sample are 20 mW and 28 mW respectively. Images were acquired in the forward detection geometry. All images are 512 x 512 pixels and acquired in 2 s. A fs pump source was used. Scale bar is 20 μm.

The image studies discussed thus far show that the miniature objective produces high contrast CARS images when detected in the forward direction. However, for tissue imaging applications, CRS signals are typically collected in the epi-direction. For generating images when detecting in the epi-direction, the objective lens needs to intercept backscattered light with a high collection efficiency. In Fig. 7(a), an epi-CARS image of a hair shaft in rabbit skin *ex vivo* is shown. The CARS signal from the hair is strong and appears with high contrast. In addition, the epi-detected SHG signal of the surrounding collagen is also shown, indicating that the miniature lens is suitable for multimodal nonlinear imaging of thick tissues. Furthermore, the excellent quality of the dual-color focal volume produced by the miniature objective also gives rise to strong SRS signals. In Fig. 7(b) an SRL image of adipocytes in the mouse ear is depicted. Similar to the CARS images, the SRL images are free from blurring and exhibit sub-micrometer lateral resolution.

Finally, we studied the strength of the CRS signal as a function of penetration depth in the tissue. For these measurements we have chosen turkey breast tissue cut to a thickness $>$ 1 mm. We collected the forward CARS signal and analyzed the decay of the coherent nonresonant background as a function of focusing depth. We find a $1/e$ decay parameter of 0.180 mm, indicating that the miniature objective is suitable for acquiring CRS images well over 100 μm deep into the tissue.

#192404 - $15.00 USD Received 17 Jun 2013; revised 3 Aug 2013; accepted 23 Aug 2013; published 19 Sep 2013

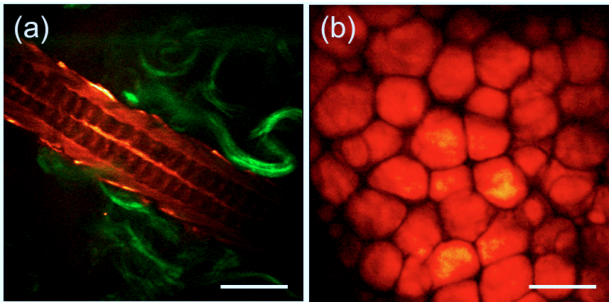

Fig. 7: Multimodal imaging of tissue samples *ex vivo* at 2845 cm^{-1} using the miniature objective (a) Epi-detection SHG (green) and CARS (red) image of thick rabbit skin tissue. A fs pump source was used. (b) Forward-detected SRS images of adipocytes in the mouse ear sample. A ps pump source was used. All images are 512 x 512 pixels. Scale bar is 20 μm.

4. Discussion and conclusion

Objectives are the most essential component in an optical probe design, and are the primary elements responsible for image quality. For CRS applications, the lens design needs to take suppression of chromatic aberrations explicitly into consideration. In systems where management of chromatic aberrations is minimum, such as in single elements aspheric lenses and in most GRIN lens designs, inferior CRS image quality may be expected. In our study, the aspheric lens, a common element in miniature probe systems, showed a reduced spatial resolution (1 ± 0.157 μm) and distortions within the field of view that can be ascribed to non-perfect overlap of the pump and Stokes beams. The aberrated performance of most single element miniature lenses in CRS imaging formed the motivation for the multi-element objective design discussed in this study.

A challenging aspect of optimizing the CRS objective with ray tracing methods is to achieve a balance between a high NA and low aberrations. By increasing the NA of the system, additional compensation is needed to keep the aberrations at tolerable levels. A design of a variety of lenses nullified the collective aberrations caused by individual optical elements such as chromatic and spherical aberrations. Another complication with increasing the NA is the shortening of the working distance. In this design we targeted an objective with a long working distance (0.872 mm), high NA (0.51) and a small diameter (5 mm) of the lens elements. The CRS imaging performance of the multi-element lens system is superior to single focusing elements, both in terms of spatial resolution and in uniformity of the CRS signal within the field of view. In fact, the resolution and image quality of the miniature lens is comparable to the imaging performance of commercial microscope objectives.

The imaging performance of the miniature lens shows that the high contrast images acquired in conventional CRS microscope systems can also be attained with optics only a fraction the size of regular microscope components. Better contrast images are imperative for making miniature CRS probes viable diagnostic tools, and the results presented in this study underline that such criteria can be realized with smaller sized optics. Nonetheless, while the current specifications are very much in line with the minimum requirements for a practical CRS probe design, there remains a future need for improving both the NA and the field of view of the system. Additionally, the ZEMAX computational design of the miniature objective could be optimized for chromatic aberration over a much broader spectral range including the visible wavelengths.

In short, we have designed, assembled and tested a 0.51 NA miniature objective for CRS imaging. The system is fully packaged and features an outer diameter of 8 mm. The lens sys-

#192404 - $15.00 USD Received 17 Jun 2013; revised 3 Aug 2013; accepted 23 Aug 2013; published 19 Sep 2013

tem shows near diffraction-limited performance with a spatial resolution sufficient for imaging subcellular details. The miniature objective is successfully used for tissue imaging, producing images with excellent CRS contrast. This work shows that it is possible to fabricate miniature lens assemblies for CRS microscopy with imaging capabilities that are comparable to the qualities of conventional microscope optics. Such capabilities will be important for the development of small probes and endoscopes, propelling the translation of CRS imaging technologies into practical clinical tools.

Acknowledgments

This work was supported by Air Force Office of Scientific Research (AFOSR, FA9550-10-1-0538), American Society for Laser Medicine and Surgery (ASLMS, S12.12, Student Research Grant), National Institutes of Health (NIH) NIBIB Laser Microbeam and Medical Program (LAMMP, P41-EB015890) and NIH K25-EB007309.

#192404 - $15.00 USD Received 17 Jun 2013; revised 3 Aug 2013; accepted 23 Aug 2013; published 19 Sep 2013